# Si Photonic-Integrated Chip Assembly With Waveguide Ge Avalanche Photodiode for 10 Gbps L-Band Optical Access Networks

Hideki Ono, *Member, IEEE*, Junichi Fujikata, Masataka Noguchi, Hiroyuki Takahashi, Masanori Itoh, Daisuke Shimura, *Member, IEEE*, Hiroki Yaegashi, and Hironori Sasaki

***Abstract*—The receiving characteristics of the silicon photonic-integrated chip assembly consisting of transimpedance amplifiers and butt-joint waveguide germanium avalanche photodiodes with lateral separated absorption and multiplication (SAM) structures were demonstrated based on conventional complementary metal-oxide-semiconductor processes. We experimentally verified a clear open eye diagram at 10 Gbps with a reverse bias of 17 V. Receiving sensitivities of −22.8 dBm and −22.0 dBm were obtained for the best and worst polarizations, respectively, with optical signals that had wavelengths longer than those of the absorption edges of Ge at a bit rate of 10 Gbps and a wavelength of 1600 nm. The proposed waveguide butt-joint germanium avalanche photodiodes with lateral SAM structures can be used to receive long wavelengths of downstream signals with low polarization dependence in next-generation optical access network systems.**

***Index Terms*—Avalanche photodiodes, optical access networks, silicon photonics.**

## I. Introduction

WITH the increase in internet traffic, the standardization of next-generation optical access network systems has become essential. L-band wavelengths are considered to be used in next-generation optical access network systems. As a result, wavelength division multiplexing with a channel spacing of 100 GHz is adopted in next-generation optical access network systems.

Photodiodes (PDs) that comprise III-V compound semiconductors with composition-dependent adjustable absorption edges are used as light-receiving devices suitable for L-band wavelengths. However, in photonic-integrated circuits fabricated by III-V compound semiconductor platforms, it is difficult to form high-precision waveguide devices compared to silicon (Si) based platforms. On the other hand, germanium (Ge) can be integrated with highly functional passive devices to form high-precision waveguides by the complementary metal-oxide-semiconductor (CMOS) process matured in large-scale integrated circuit manufacturing platforms. However, Ge monolithically integrated by Si photonics technology does not show high responsivity at the L-band wavelength owing to its absorption edge at approximately 1550 nm.

To solve this problem, several methods have been reported to narrow the band gap of Ge absorbers. The application of stress to the Ge absorber has been demonstrated [1], [2], [3]. Another approach is to alloy the Ge absorber with GeSn [4] and [5]. However, these techniques do not allow mass production and are incompatible with the CMOS process. Therefore, we have been developing PDs compatible with the CMOS process and can provide high responsivity at the L-band wavelength. We first developed Ge PDs with a p-i-n (PIN) structure comprising an aligned p region, an intrinsic region, and an n region in the lateral (L) direction [6]. We then developed Ge avalanche photodiodes (APDs) with a separated absorption and multiplication (SAM) structure comprising an aligned p region and n region in the L direction [7]. These structures allow the detection of L-band optical signals with high responsivity because the optical signals propagating in Ge are not scattered and absorbed by metal electrodes since no electrodes are formed on the Ge absorber. The longer device length leads to higher responsivity, realizing L-band optical signal detection.

Since the polarization state of the optical signal randomly changes in the single-mode fiber used in optical access networks, the responsivity must be independent of the polarization state. To fulfill this requirement, we developed a Ge PIN PD and Ge APD where the optical coupling between the Si waveguide (WG) and the Ge absorber is butt-joint (BJ). We verified that the dependence of responsivity on polarization in the BJ structure was smaller than that of the evanescent

Manuscript received 24 August 2022; accepted 25 August 2022. Date of publication 1 September 2022; date of current version 12 September 2022. This work was supported by New Energy and Industrial Technology Development Organization through the results obtained from a Project under Grant JPNP13004. *(Corresponding author: Hideki Ono.)*

Hideki Ono, Hiroyuki Takahashi, Daisuke Shimura, Hiroki Yaegashi, and Hironori Sasaki are with the Sensing Technologies R&D Department, Innovation Promotion Center, Oki Electric Industry Company, Ltd., Warabi 335-8510, Japan, and also with Photonics Electronics Technology Research Association, Tsukuba, Ibaraki 305-8569, Japan (e-mail: ono465@oki.com; takahashi276@oki.com; shimura273@oki.com; yaegashi454@oki.com; sasaki437@oki.com).

Junichi Fujikata is with the Graduate School of Technology, Industrial and Social Sciences, Tokushima University, Tokushima 770-8506, Japan, and also with the Photonics Electronics Technology Research Association, Tsukuba, Ibaraki 305-8569, Japan (e-mail: fujikata.junichi@tokushima-u.ac.jp).

Masataka Noguchi is with Secure System Platform Research Laboratories, NEC Corporation, Tsukuba, Ibaraki 305-8560, Japan, and also with Photonics Electronics Technology Research Association, Tsukuba, Ibaraki 305-8569, Japan (e-mail: masataka.noguchi@aist.go.jp).

Masanori Itoh is with the Sensing Technologies R&D Department, Innovation Promotion Center, Oki Electric Industry Company, Ltd., Warabi 335-8510, Japan (e-mail: itoh176@oki.com).

Digital Object Identifier 10.1109/JPHOT.2022.3202575

This work is licensed under a Creative Commons Attribution 4.0 License. For more information, see https://creativecommons.org/licenses/by/4.0/

coupling one. As a result, we hypothesized that BJ-WG-L-SAM-Ge-APD would be suitable for high-speed L-band optical signal detection, and we further optimized the size of each region.

In this work, we report experimental results and discuss their dark current, responsivity, and frequency response characteristics. We show the dependence of device responsivity on wavelength, reverse bias, and optical input power. The frequency response dependence on reverse bias and optical input power is also reported at the L-band wavelength. We also assembled BJ-WG-L-SAM-Ge-APDs with a transimpedance amplifier (TIA) and investigated their applicability to optical network units (ONUs) in next-generation optical access networks, such as time wavelength division multiplexing-passive optical network (TWDM-PON). Although the sensitivity defined in ITU-T [8] was not completely achieved, the characteristics were significantly improved compared to the transceiver module using the Ge PIN PD [9].

## II. Design and Fabrication

The design concept is as follows: The Ge absorber lies in contact with the p-Si region and the i-Si multiplication region, which is in contact with the n-Si region. It is well-known that high speed and low noise are obtained when carriers are multiplied in the material that has a large or close to zero ionization coefficient ratio, $\kappa\,(=\beta/\alpha,\ \alpha$: ionization coefficient of electrons, $\beta$: ionization coefficient of holes), in APDs. Electrons reach the edge of the avalanche region in the depletion region while repeating ionization in the case of $\alpha \gg \beta$. On the other hand, holes drift in the avalanche region in the reverse direction of electrons and exit from the avalanche region. Therefore, hole ionization almost does not occur. For this reason, the excess noise is very small because the generation of multiplied carriers almost ends when injected electrons pass through the avalanche region. The corresponding excess noise becomes the smallest in the case of either the injection of electrons at $\alpha \gg \beta$ or holes at $\alpha \ll \beta$. However, in the case of $\alpha \approx \beta$, holes generated by ionization drift in the direction opposite to the electron drift direction and lead to ionization again. Because the electrons generated at this time cause ionization as the first electrons, the chain reaction of ionization continues. Therefore, the excess noise is large due to large output current variation because the multiplication ratio per one carrier is substantially large [10].

Based on the above considerations, we determined the polarity of p-n so that electrons can be multiplied in Si, which has $\alpha \gg \beta$ $(\kappa < 0.1)$[11], not in Ge in which $\alpha \approx \beta\ (\kappa \approx 2)$[12]. As shown in Fig. 1, the photocarriers generated in the Ge absorber are electrons and holes separated by the electric field. The holes drift to the p-Si region. On the other hand, the electrons are multiplied in the i-Si multiplication region by avalanche multiplication before reaching the n-Si region.

In this work, the BJ-WG-L-SAM-Ge-APDs were fabricated using the same methods described in [7]. The silicon-on-insulator (SOI) wafers with a Si substrate thickness of 775 $\mu$m, a buried oxide (BOX) layer thickness of 3 $\mu$m, and an SOI layer thickness of 200 nm were used in CMOS facilities for

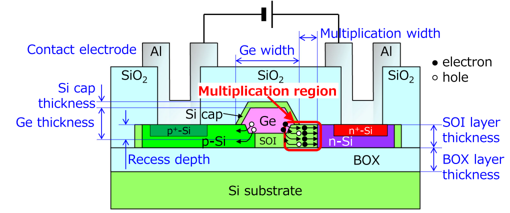


Fig. 1. Cross section of the BJ-WG-L-SAM-Ge-APD.

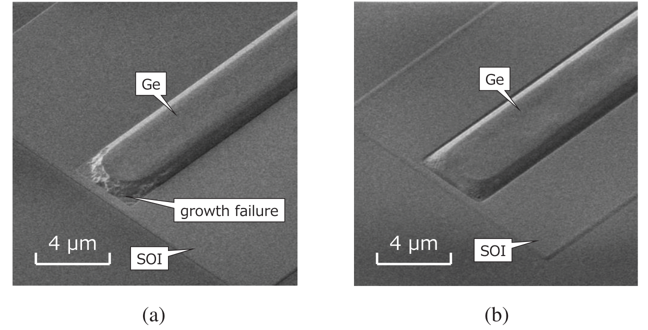


Fig. 2. Scanning electron microscopy image of the selective epitaxial growth of the Ge absorber used in this work.

300-mm-diameter wafers. The Ge thickness and the recess depth were 500 nm and 70 nm, respectively.

In this work, we used ultrahigh-vacuum chemical vapor deposition (UHV-CVD) for the selective epitaxial growth of Ge. However, as shown in Fig. 2(a), the selective epitaxial growth of Ge with a narrow width and a long absorption length increases the probability of growth failure. Since the growth failure of the Ge absorber causes scattering loss during the propagation of optical signals through the Ge absorber and trap photocarriers, the surface of the Ge absorber must be smooth. Therefore, we investigated selective epitaxial growth conditions, such as gas flow rate and the pretreatment of the growth window, to reduce the growth failure of Ge. Further, we increased the thickness of the Si cap in Fig. 1 to 30 nm or more. As a result, as shown in Fig. 2(b), the Ge absorber with a long absorption length and a smooth surface was obtained.

## III. Evaluation

### A. Device Characteristics

*1) Dark Currents:* Fig. 3 shows the measurement result of the dark current-voltage characteristics of the APD with a Ge width of 1 $\mu$m, a Ge absorption length of 200 $\mu$m, and a multiplication width of 0.4 $\mu$m, where the reverse voltage at the reverse current of 10 $\mu$A is defined as the breakdown voltage $V_{BR}$. The reverse current at 90% of $V_{BR}$ is defined as the dark current $I_D$ and is found to be 8.29 $\mu$A. This value is significantly larger than other reported Ge APDs [13], [14], [15], [16], [17]. The dark current per unit length is also large. This relatively large dark current may be caused by the presence of many dislocation defects found in the Ge absorber, especially in the boundary between the Ge absorber and the SOI layer. Since the direction in which the defects are aligned in the boundary and the direction of the

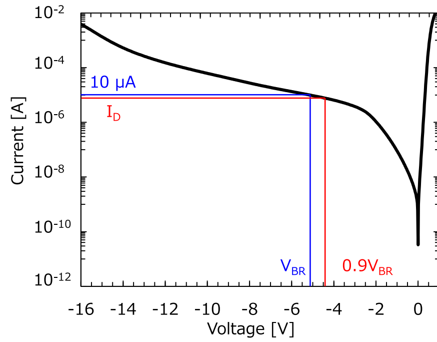


Fig. 3. Dark current versus voltage.

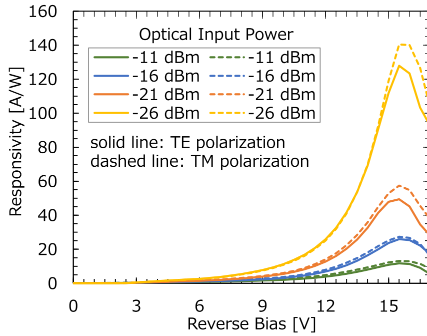


Fig. 4. Responsivity versus reverse bias for each optical input power and polarization at a wavelength of 1600 nm.

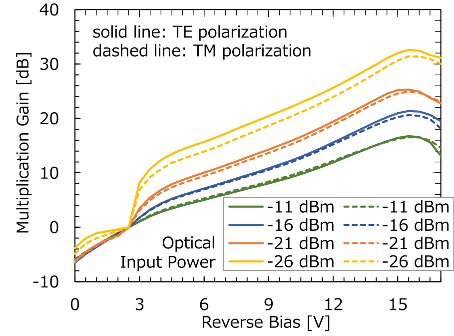


Fig. 5. Multiplication gain versus reverse bias for each optical input power and polarization at a wavelength of 1600 nm.

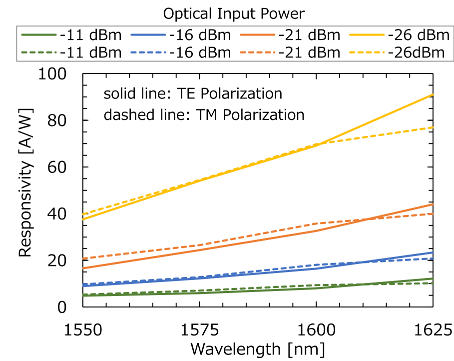


Fig. 6. Responsivity versus wavelength for each optical input power and polarization at a reverse bias of 14 V.

electric field coincide with each other, it is more difficult to suppress the reverse current due to crystal defects in the L Ge PDs than in the vertical (V) Ge PDs. Therefore, it is important to find the best composition of the buffer layer between the Ge absorber and the SOI layer to reduce the dark current, $I_D$.

*2) Responsivity:* In this work, to measure the responsivity, a tunable wavelength light source (Agilent 81940 A), an optical power meter (Agilent 81634 A), and a power source current meter (Agilent B2912 A) were used. The optical power input $P_{in}$ to the Ge APD was determined beforehand by measuring the propagation loss of the Si WG of the Si photonics (SiP) chip and the coupling loss between the Si WG and the tip-sphere fiber at each wavelength, polarization, and optical power. Under each condition, the current output $I_{out}$ from the Ge APD was measured at each bias, and the current $I_p$ was obtained by subtracting the dark current from $I_{out}$ as the true photocurrent. Finally, the responsivity was calculated as $I_p/P_{in}$.

Fig. 4 shows the measurement results of the dependence of the responsivity on the reverse bias applied to the BJ-WG-L-SAM-Ge-APD of the same dimension described in previous section *1) Dark Currents*, at the wavelength of 1600 nm for different optical input powers. The responsivity linearly increased with the increase in the reverse bias from 0 to 2.5 V, and it exponentially increased as the reverse bias increased from 2.5 to 14 V, indicating that the multiplication occurred at a reverse bias of 2.5 V or higher. Considering the dark current characteristics shown in Fig. 3, it seems that punch-through occurred at a reverse bias of 2.5 V. The maximum responsivities of 127.9 A/W and 140.4 A/W were obtained at a reverse bias of 15.5 V and an input optical power of −26 dBm for TE and TM polarization states, respectively. To date, the highest responsivity at a wavelength of 1600 nm was obtained in the WG-Ge-APDs with low polarization dependence [13] and [18] since optical coupling between the Si WG and the Ge absorber was BJ. By calculation from the measured responsivity, the maximum gain was 32.6 dB at TE polarization and 31.4 dB at TM polarization at an optical input power of −26 dBm, as shown in Fig. 5. The responsivity decreased over a reverse bias of 15.5 V because both phonon scattering and the space charge effect occurred due to the increase in the carrier density [16].

Fig. 4 shows that the responsivity reduced as the optical input power increased, as reported by Virot et al. [16]. Also, as shown in Fig. 5, the maximum gain increased as the optical input power decreased. For example, the maximum gain decreased by 5 dB when the optical input power increased by 5 dB. This is likely due to phonon scattering and the space charge effect as described above.

Fig. 6 shows the measurement results of the dependence of the responsivity on wavelength in the range of 1550–1625 nm for different optical input powers at a reverse bias of 14 V. Fig. 7 shows the dependence of the multiplication gain on wavelength from 1550 nm to 1625 nm in the same case. From both figures, we found that the APD had a lower responsivity multiplication gain in the C-band wavelength than in the L-band wavelength because of phonon scattering and the space charge effect as

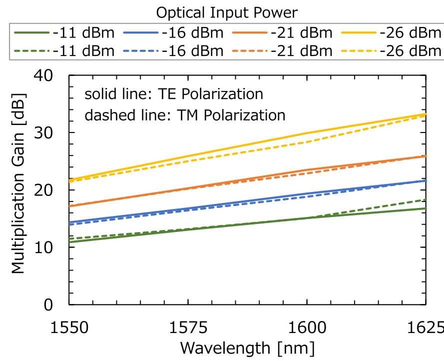


Fig. 7. Multiplication gain versus wavelength for each optical input power and polarization at a reverse bias of 14 V.

described above. Since the absorption coefficient of Ge in the C-band wavelength is higher than that in the L-band wavelength, optical carriers are generated intensively near the entrance of the Ge absorber for the input optical signal. As a result, the space charge effect is more pronounced in the C-band wavelength than in the L-band wavelength; thus, the responsivity is lower in the C-band wavelength than in the L-band wavelength.

As shown in Fig. 6, the polarization dependence of the responsivity was larger at a wavelength of 1625 nm. Since the polarization dependence of the responsivity at punch-through (reverse bias: 2.5 V), which is used as a reference for the gain, was also large, the polarization dependence of the gain was small, as shown in Fig. 7. In Fig. 6, the polarization dependence of the responsivity increased with the wavelength. This may be due to the propagation loss of the Ge WG caused by the asymmetry of the Ge cross section when the Ge absorber was used as a WG.

*3) Cut-Off Frequency:* In this work, a light wave component analyzer (Agilent N4373D) and a network analyzer (Agilent N5227 A) were used to measure the frequency response. Since the light wave component analyzer did not have a light source with a wavelength of 1600 nm, the light source with tunable wavelengths used for the responsivity measurement was used as an external light source. Similarly, the same power source current meter as in the responsivity measurement was used for bias application, and the same optical power meter as in the responsivity measurement was used for optical power measurement. The optical power input $\mathrm{P_{in}}$ to the Ge APD at each polarization and optical power was measured beforehand. Under each condition, the optoelectric response parameter $\mathrm{S_{41}}$ was measured at each bias, and from the result of the normalization of $\mathrm{S_{41}}$ with the lowest frequency of 10 MHz as 0 dB, the 3 dB down frequency was obtained as the cut-off frequency.

Fig. 8 shows the cut-off frequency characteristics obtained from the measurement of small signal responses of the APD of the same dimension described in previous section *1) Dark Currents*, at a wavelength of 1600 nm. As shown in Fig. 8, the cut-off frequencies were about 10 GHz independent of the optical input power. Although the cut-off frequency is sufficient for TWDM-PON applications, the response of the BJ-WG-L-SAM-Ge-APD in this work is inferior to other previously

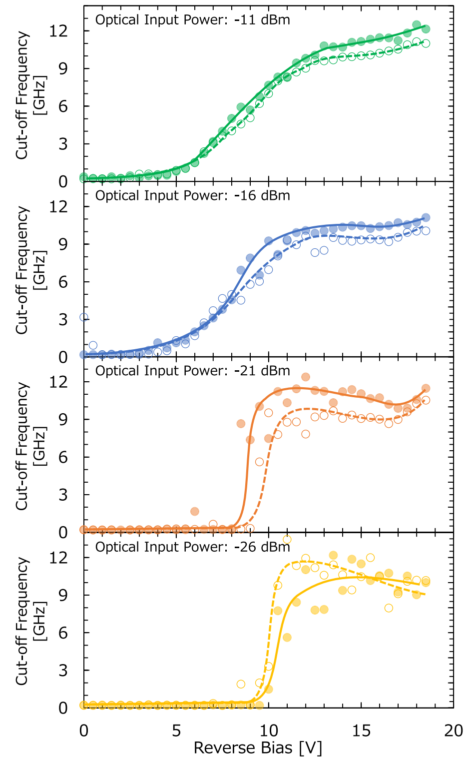


Fig. 8. Cut-off frequency versus reverse bias for each optical input power and polarization at a wavelength of 1600 nm.

reported WG-Ge-APDs [13], [17], [18], [19], [20] in which cut-off frequencies were nearly equal to or more than 30 GHz. The lower cut-off frequency may be due to the longer distance between the p-Si and the n-Si regions of the Ge APD compared to other Ge APD structures reported in the literature. As a result, the transit time of photocarriers and the CR time constant increase due to the wider width of the high-resistance i-Si region. To improve the cut-off frequency while maintaining the structure of the BJ-WG-L-SAM-Ge-APD, the device design needs to be adjusted at the expense of the multiplication gain.

The relationship between the reverse bias voltage and the frequency response varies depending on the optical input power. For the optical input powers of −11 and −16 dBm, the frequency response began to appear at 3 V of the reverse bias. The cut-off frequency gradually increased as the reverse voltage increased up to 12 V, followed by a slight increase in the cut-off frequency at reverse biases above 12 V. For the optical input power of −21 dBm, the frequency response rapidly increased between 8 and 9 V of the reverse bias. The cut-off frequency peaked at a reverse bias of 12 V and slightly decreased as the reverse bias increased further. Then, the cut-off frequency again increased with the reverse bias of more than 17 V. For the optical input power of −26 dBm, the frequency response suddenly appeared around 10 V of the reverse bias. The cut-off frequency peaked at around 12 V of the reverse bias and slowly decreased above 12 V of the reverse bias similar to the case of −21 dBm optical input power.

As shown in Fig. 8, the cut-off frequency behaved differently at low and high optical input powers. At −21 dBm, the trends

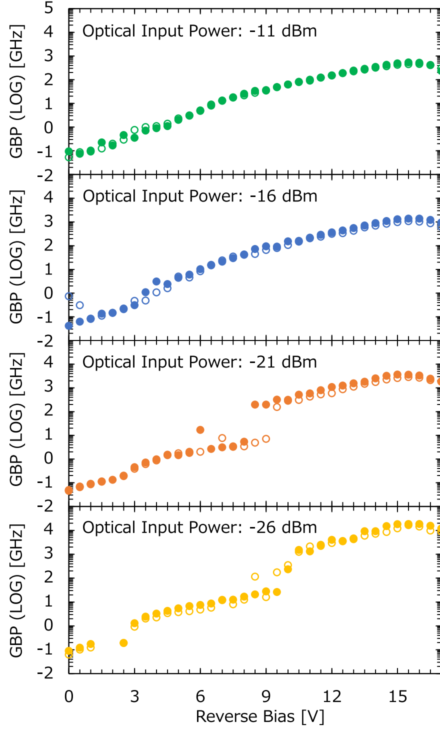


Fig. 9. Dependence of gain bandwidth product characteristics on reverse bias.

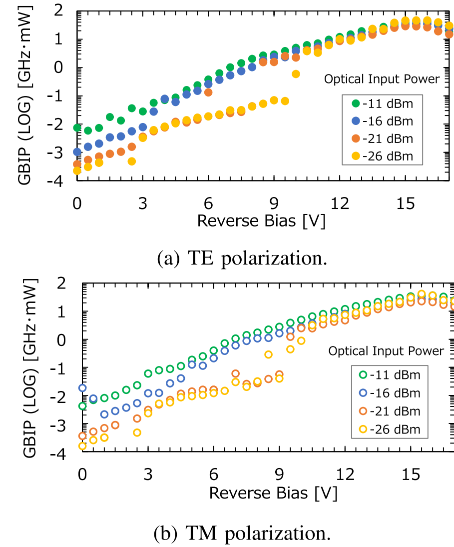


(a) TE polarization.

(b) TM polarization.

Fig. 10. Dependence of gain, bandwidth, and input power (GBIP) characteristics on reverse bias.

seen for −16 dBm and −26 dBm seemed to overlap; the abrupt increase in the cut-off frequency occurred at a reverse bias of 10 V, and the cut-off frequency further increased for the reverse bias larger than 17 V.

We deduce that the dependence of the cut-off frequency on the reverse bias and the optical input power can be explained as follows: Beyond −16 dBm, the electrical resistance of the Si multiplication region is small, and the CR time constant is small because the quantity of carriers generated in the Ge optical absorption region is large despite the low reverse bias. Therefore, the frequency response is observed even if the multiplication in the Si multiplication region does not occur. The reason that the cut-off frequency shows a slight increase beyond 12 V may be because the cut-off frequency of the Ge optical absorption region continues to increase despite the multiplication saturation in the Si multiplication region. On the other hand, for −26 dBm, the electrical resistance of the Si multiplication region is large, and the CR time constant is also large because the quantity of carriers generated in the Ge optical absorption region is small. Therefore, the frequency response is observed only when the multiplication occurs in the Si multiplication region. The reverse bias at which the multiplication begins in the Si multiplication region is in the range of 8–10 V, and the cut-off frequency decreases slowly due to the multiplication saturation in the Si multiplication region beyond 12 V.

*4) Gain Bandwidth Product (GBP):* Fig. 9 shows the dependence of the GBP characteristics on the reverse bias applied to our SAM-APD at 1600 nm, obtained from Figs. 5 and 8. Although the measuring wavelengths were different from ours, GBPs previously reported in [17] and [21] were 383 GHz and 276 GHz, respectively, and a higher GBP was obtained in this work for the BJ-WG-L-SACM-Ge-APD. As shown in Fig. 9, the GBP increased when the optical input power decreased. The maximum GBP value was 534 GHz at −11 dBm, 1402 GHz at −16 dBm (at 15.5 V of reverse bias for each optical input power), 3641 GHz at −21 dBm (at 15 V of reverse bias), and 18447 GHz at −26 dBm (at 16 V of reverse bias) for TE polarization. In other words, the variation in the GBP was 15.4 dB with an optical input power decrease of 15 dB. This may indicate a clear relationship between the maximum GBP value and the optical input power.

As shown in Fig. 9, there are discontinuous points of dependence of the GBP on the applied reverse bias for optical input powers smaller than −21 dBm. It is obvious that these discontinuous points are associated with the discontinuity of the frequency response, as shown in Fig. 8, because the discontinuous points of the GBP appear at the same reverse bias of the frequency response. The reason for this discontinuity is that the multiplication begins in the Si multiplication region at the reverse bias range of 8–10 V.

Since the GBP characteristics depend on the optical input power, we defined the gain, bandwidth, and input power (GBIP) by multiplying the GBP by the optical input power. The GBIP as a function of reverse bias are shown in Fig. 10. As shown in Fig. 10(a), for TE polarization, the maximum GBIP obtained in the high-reverse-bias region of 15.5 V was 46.3 GHz mW, 28.8 GHz mW, 35.2 GHz mW and 42.4 GHz mW at −26 dBm, −21 dBm, −16 dBm, and −11 dBm, respectively. In brief, the GBIP change was only 2.1 dB, while the optical input power increased by 15 dB from −26 dBm to −11 dBm. As described above, in the APD performance evaluation, the optical input power dependence can be disregarded by calculating the GBIP.

## *B. Optical Receiving Characteristics*

*1) Assembling TIA and APD:* Fig. 11 shows the overview of the assembly prototyped by mounting a TIA and a SiP chip

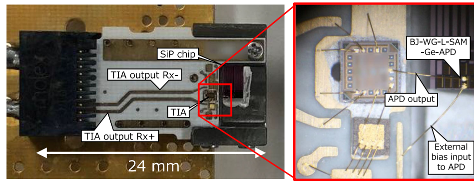


Fig. 11. Assembly of TIA and APD evaluated in this work.

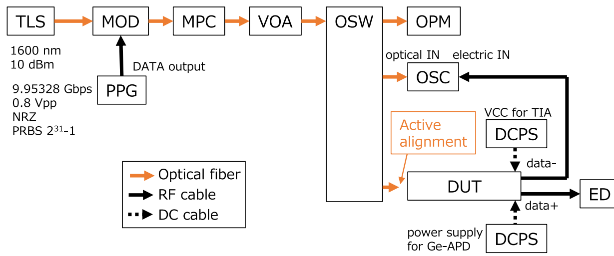


Fig. 12. Configuration for the evaluation of the TIA and APD assembly (TLS: tunable laser source, MOD: optical modulator, MPC: manual polarization controller, VOA: variable optical attenuator, OSW: optical switch, OPM: optical power meter, OSC: sampling oscilloscope, DUT: device under test, DCPS: dc power supply, PPG: pulse pattern generator, ED: error detector).

including the APDs proposed in this work onto a printed circuit board. On the SiP chip, simple spot size converters (SSCs) with a narrow tip width (220 nm), Si WGs (480 nm width), and the APDs were integrated. We formed a rectangular Si WG cross section (width/height = 480 nm/200 nm) to maintain the linear polarization of optical signals in the Si WGs. The optical input was achieved by the active alignment between the polarization maintaining a spherical lensed fiber and the SSC on the edge face of the SiP chip. The spherical lensed fiber was not fixed on the assembly, and no refractive-index-matching material such as matching oil was used. In this case, the optical coupling loss between the polarization maintaining the spherical lensed fiber and the SSC was estimated to be about 1.6 dB at 1600 nm, independent of the polarization state. The APD and the TIA were electrically connected through gold (Au) wires. The TIA and the printed board were electrically connected similarly. The TIAs (GigOptix HXR4101 A) used in this work could not provide a sufficient reverse bias voltage to the APDs since they were commercial products. Therefore, necessary reverse biases were separately applied to the APDs directly from the printed board through an Au wire without using the TIA power port since the assembly in this work was intended for a single-channel receiving operation. For the 4-channel 10 Gbps receiving operation required by the full operation of TWDM-PON, it is necessary to develop a TIA with 4 channels of external bias terminals to provide high bias to APDs.

*2) Large Signal Response:* Fig. 12 shows the configuration used to evaluate the assembly based on the input optical signal of 10 Gbps, non-return-to-zero (NRZ), and pseudo-random binary sequence of $2^{31}-1$ at 1600 nm. Fig. 13 shows the eye diagram of the input optical signal measured by a sampling oscilloscope with an average power of 0.6 dBm. The extinction ratio was 12.25 dB, and the signal-to-noise ratio (SNR) was 15.76.

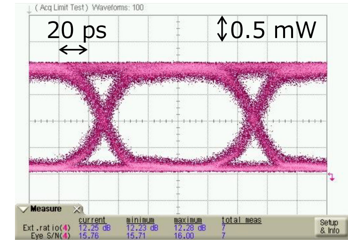


Fig. 13. Eye diagram of the input optical signal with an average power of 0.6 dBm.

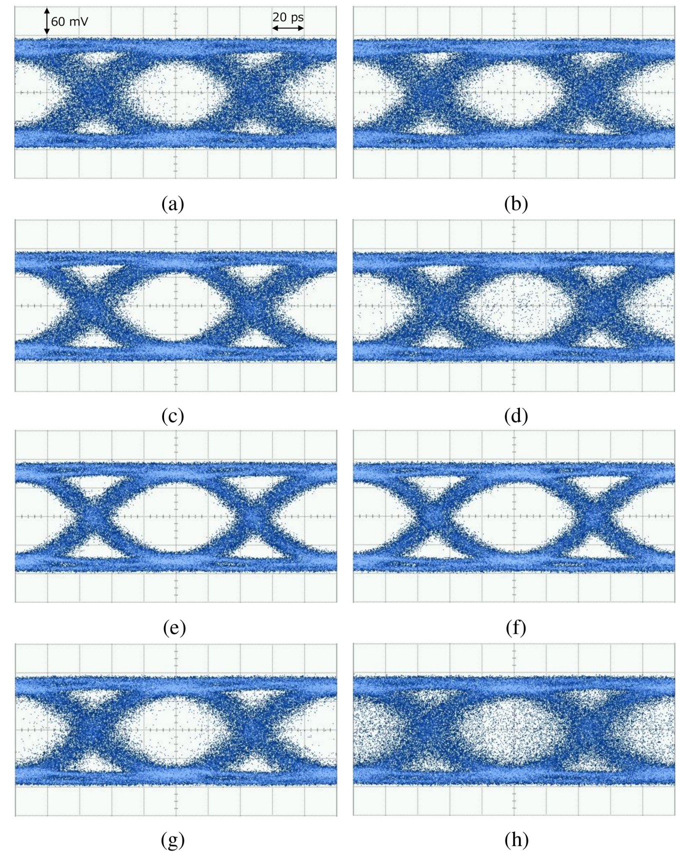


Fig. 14. Measured eye diagrams of the assembly proposed in this work for the best and the worst polarizations. {(a) Reverse bias: 8 V, Optical input power: −7.6 dBm, Polarization: Best / (b) Reverse bias: 8 V, Optical power: −7.6 dBm, Polarization: Worst / (c) Reverse bias: 12 V, Optical power: −12.6 dBm, Polarization: Best / (d) Reverse bias: 12 V, Optical power: −12.6 dBm, Polarization: Worst / (e) Reverse bias: 17 V, Optical power: −13.6 dBm, Polarization: Best / (f) Reverse bias: 17 V, Optical power: −13.6 dBm, Polarization: Worst / (g) Reverse bias: 18 V, Optical power: −17.6 dBm, Polarization: Best / (h) Reverse bias: 18 V, Optical power: −17.6 dBm, Polarization: Worst}.

Fig. 14 shows the eye diagrams of the output voltage from the TIA of the assembly under various conditions. For low reverse bias conditions, clear eye openings were not observed as many signal points existed in the eye opening despite the sufficient eye amplitude.

These results indicated that the current inflowing to the TIA was large enough to enable the auto-gain control of the TIA due to the large dark current. In addition, the dark currents were too large, contrary to multiplication gain. The SNRs of the eye

diagrams at the best polarization in Fig. 14(a)–(d) were 7.66 dB, 7.72 dB, 9.18 dB, and 7.23 dB, respectively. On the other hand, as shown in Fig. 14(g) and (h), many signal points existed in the eye opening, and clear eye opening was not observed for the high reverse bias due to low multiplication gain. The SNRs of the eye diagrams at the worst polarization in Fig. 14(g) and (h) were 8.85 dB and 5.30 dB, respectively.

As shown in Fig. 14(e) and (f), any signal points did not exist in the eye opening, and clear eye openings were observed with the optimum reverse bias of 17 V, regardless of polarization. These results indicate that the BJ-WG-L-SAM-Ge-APDs developed in this work are suitable for receivers with a wavelength of 1600 nm and a transmission rate of 10 Gbps. The SNRs of the eye diagrams in Fig. 14(e) and (f) were 9.67 dB and 9.68 dB, respectively. These results indicate that the SNR increases as the reverse bias approaches the optimum value. In other words, comparing the dependence of the dark current and gain on the reverse bias, we found that the increase in gain is dominant until the optimum reverse bias.

*3) Bit Error Rate (BER):*

*a) Theoretical Discussion:* In intensity modulation-direct detection (IM-DD), assume that the mark signal follows a Gaussian distribution with the mean level $S_1$ and variance $\sigma_1^2$, and the space signal follows a Gaussian distribution with the mean level $S_0$ and variance $\sigma_0^2$. Then, the factor $Q$, which represents the quality of the discriminant circuit input signal, is expressed by the following equation:

$$Q = \frac{S_1 - S_0}{\sigma_1 - \sigma_0} \tag{1}$$

The BER is expressed by the following equation [22]:

$$BER = \frac{1}{2} erfc\left(\frac{Q}{\sqrt{2}}\right) \tag{2}$$

where $erfc$ is the complementary error function. The SNR power ratio of the input signal is given by $SNR = 4Q^2$, the BER is given as a function of SNR as

$$BER = \frac{1}{2} erfc\left(\frac{\sqrt{SNR}}{2\sqrt{2}}\right) \tag{3}$$

However in this work, the SNR of the APDs was described as follows [23]:

$$SNR = \frac{I_L^2 \quad M^2}{2q(I_L + I_{DG})BM^2F + 2qI_{DS}B + \dfrac{4kTB}{R_L}} \tag{4}$$

In (4), the primary mean dark-generated current is divided into the dark current $I_{DG}$ and the dark current $I_{DS}$. For example, $I_{DG}$ is the reverse saturation current through defect states related to crystal defects or impurities in the intrinsic region, and $I_{DS}$ is the surface leakage current not related to the photoelectric effect inside the APDs. The mean multiplications of the photoinjected and dark-generated carriers are set to be equal to $M$. The excess noise factors of the photoinjected current and the dark-generated current are set to be equal to $F$. The variance of the circuit noise is expressed by the load resistance $R_L$. $I_L$ is the photoinjected current at $M = 1$, $q$ is the electronic charge, $B$ is the signal bandwidth, $k$ is the Boltzmann's constant, and $T$ is the absolute

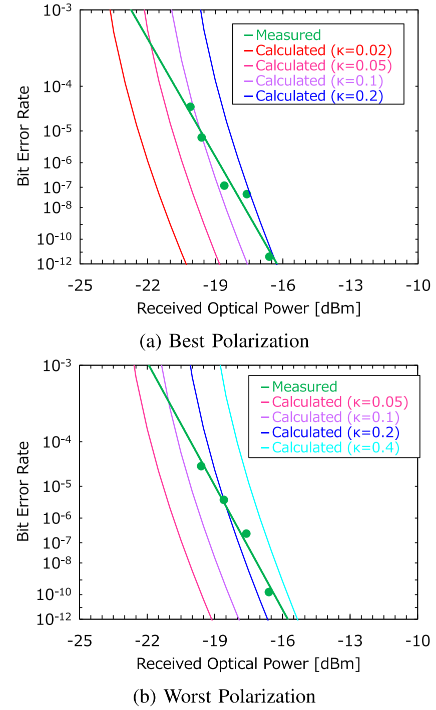


Fig. 15. Measured and calculated BERs versus received optical power in the Ge APD.

temperature, respectively. The excess noise factor $F$ is expressed by the following equation:

$$F = M\kappa + \left(2 - \frac{1}{M}\right)(1 - \kappa) \tag{5}$$

where $\kappa$ is the hole-to-electron ionization rate ratio. According to the report by Kang et al. [11], $\kappa$ of Si is less than 0.1. On the other hand, $\kappa$ of Ge varies from 1.5 to 4 [12]. Using (3)–(5), the BER of the BJ-WG-L-SAM-Ge-APDs was calculated.

*b) Results:* Fig. 15 shows the BER measurement results of the assembly shown in Fig. 11 at a reverse bias of 17 V with eye diagrams shown in Fig. 14(e) and (f). The sensitivity of the assembly was found to be $-22.8$ dBm in the best polarization state and $-22.0$ dBm in the worst polarization state at the BER reference level of $10^{-3}$. Based on the above APD sensitivity, the corresponding sensitivity of the optical subscriber terminal was estimated in the range of $-17.0$ to $-17.8$ dBm, taking into account an additional insertion loss of about 5 dB for the wavelength multiplexing/demultiplexing filter. The measured sensitivities of our transceiver module using the Ge PIN PD previously reported in [9] were $-1$ dBm at TE polarization and 0 dBm at TM polarization. Therefore, the BJ-WGL-SAM-Ge-APD improved the receiving sensitivity at the L-band wavelength by more than 16 dB. For next-generation access networks such as TWDM-PON ONU [8], since ITU-T defines $-28$ dBm as the sensitivity specification of subscriber terminals, an additional sensitivity improvement of more than $-11$ dB is required.

Fig. 15 shows the BER calculation results assuming various values of $\kappa$. Although the signal bandwidth was 10 GHz since the signal was NRZ, $B$ was set to 5 GHz, and $T$ was set to 298.15 K.

It is difficult to obtain the precise value of both $I_{DG}$ and $I_{DS}$ from the measurement results. For calculations, $I_{DS}$ was set to the dark current at the reverse bias of 1 V, and $I_{DG}$ was set to the dark current at the reverse bias at $M = 1$. Fig. 15 shows that $\kappa$ becomes larger when the optical receiving power is high. Since $\kappa$ in Si is about 0.1 and $\kappa$ in Ge is about 2, Fig. 15 shows that the multiplication occurs mainly in Si when the optical input power is small, whereas the multiplication in Ge increases as the optical input power increases.

As deduced from Fig. 13, lowering the dark current of the BJ-WG-L-SAM-Ge-APD is one of the most effective approaches to improving sensitivity. A TWDM-PON ONU sensitivity specification may be realized by reducing the dark current by an order of magnitude or more. We are currently considering further reduction of receiving sensitivity in the assembly by lowering the dark current. For dark current reduction, the first approach is to improve the crystallinity of the Ge absorber, and the second approach is to reduce the dislocation defects in the buffer layer between Ge and Si by the optimization of the buffer layer composition. In addition, the design of the SAM structure, including the width and position of the multiplication region, is modified to improve the responsivity at $M$=1 and optimize the multiplication gain. Reducing $\kappa$ and decreasing $F$ is also effective for improving sensitivity. Therefore, we are currently developing Ge APDs with a separated absorption, charge, and multiplication (SACM) structure to efficiently multiplicate optical carriers in only Si.

## IV. Summary

We fabricated and evaluated the BJ-WGL-SAM-Ge-APDs compatible with the conventional CMOS process to reduce the polarization dependence of the responsivity by the BJ structure. Although the dark current was relatively large, the highest responsivity at the L-band wavelength was experimentally demonstrated with low polarization dependence. In addition, we evaluated eye diagrams and BERs by 10 Gbps optical signal input at the L-band wavelength by assembling a prototype of the WG-BJ-L-SAM-Ge-APD and a commercially available TIA and confirmed applicability to the subscriber terminal in next-generation optical access network systems. Further improvement of device sensitivity is under development.

## References

[1] L. Ding, T. Y. Liow, A. E. J. Lim, N. Duan, M. B. Yu, and G. Q. Lo, "Ge waveguide photodetectors with responsivity roll-off beyond 1620 nm using localized stressor," in *Proc. Opt. Fiber Commun. Conf./Nat. Fiber Opt. Eng. Conf.*, 2012, Paper OW3G.4.

[2] D. Feng et al., "Horizontal p-i-n high-speed Ge waveguide detector on large cross-section SOI waveguide," in *Proc. Opt. Fiber Commun. Conf./Nat. Fiber Opt. Eng. Conf.*, 2010, Paper OWN2.

[3] R. Anthony et al., "Extended wavelength responsivity of a germanium photodetector integrated with a silicon waveguide exploiting the indirect transition," *IEEE J. Sel. Topics Quantum Electron.*, vol. 26, no. 2, Mar./Apr. 2020, Art. no. 3800107.

[4] M. Oehme et al., "GeSn-on-Si normal incidence photodetectors with bandwidths more than 40 GHz," *Opt. Exp.*, vol. 22, no. 1, pp. 839–846, Jan. 2020.

[5] H. Cong et al., "Silicon based GeSn p-i-n photodetector for SWIR detection," *IEEE Photon. J.*, vol. 8, no. 5, Oct. 2016, Art. no. 6804706.

[6] H. Ono, T. Simoyama, S. Okumura, M. Imai, H. Yaegashi, and H. Sasaki, "Waveguide butt-joint germanium photodetector with lateral PIN structure for 1600 nm wavelengths receiving," *IEICE Trans. Electron.*, vol. E 101-C, no. 6, pp. 409–415, Jun. 2018.

[7] H. Ono et al., "Si photonics butt-coupled waveguide germanium avalanche photodiodes with lateral SAM structures," *Opt. Fiber Commun. Conf.*, 2019, Paper Th3A.9.

[8] ITU-T G.989.2. [Online]. Available: https://www.itu.int/rec/dologin_pub.asp?lang=e&id=T-REC-G.989.2-202010-I!Amd1!PDF-E&type=items

[9] H. Ono et al., "Receiver characteristics of 4ch transceiver module with Si photonics integrated chip suitable for TWDM-PON ONU," in *Proc. 24th Optoelectron. Commun. Conf.*, 2019, Paper WD3-3.

[10] R. J. McIntyre, "Multiplication noise in uniform avalanche diodes," *IEEE Trans. Electron Devices*, vol. ED-13, no. 1, pp. 164–168, Jan. 1966.

[11] Y. Kang et al., "Monolithic germanium/silicon avalanche photodiodes with 340 GHz gain-bandwidth product," *Nature Photon. Lett.*, vol. 3, no. 1, pp. 59–63, Dec. 2008, doi: 10.1038/NPHOTON2008.247.

[12] J. Lee, A. L. Gutierrez-Aitken, S. H. Li, and P. K. Bhattacharya, "Impact ionization coefficients in $Si_{1-x}Ge_x$," *Appl. Phys. Lett.*, vol. 66, no. 2, pp. 204–205, Jan. 1995.

[13] T. Y. Liow, A. E. J. Lim, N. Duan, M. Yu, and G. Q. Lo, "Waveguide germanium photodetector with high bandwidth and high L-band responsivity," in *Proc. Opt. Fiber Commun. Conf.*, 2013, Paper OM3K.2.

[14] Y. Zhang et al., "A high-responsivity photodetector absent metal-germanium direct contact," *Opt. Exp.*, vol. 22, no. 9, pp. 11367–11375, May 2014.

[15] J. Zhang, B. Ping-Piu Kuo, and S. Radic, "64 Gb/s PAM4 and 160 Gb/s 16QAM modulation reception using a low-voltage Si-Ge waveguide-integrated APD," *Opt. Exp.*, vol. 28, no. 16, pp. 23266–23273, Aug. 2020.

[16] L. Virot et al., "Germanium avalanche receiver for low power interconnects," *Nature Commun.*, vol. 5, Sep. 2014, Art. no. 4957, doi: 10.1038/ncomms5957.

[17] Y. Xiang, H. Cao, C. Liu, and D. Dai, "High-performance waveguide Ge/Si avalanche photodiode with a lateral separate-absorption-charge-multiplication structure," *Opt. Exp.*, vol. 30, no. 7, pp. 11288–11297, Mar. 2022.

[18] K. Takeda et al., "Contributions of Franz-Keldysh and avalanche effects to responsivity of a germanium waveguide photodiode in the L-band," *IEEE J. Sel. Topics Quantum Electron.*, vol. 20, no 4, Jul./Aug. 2014, Art. no. 3800507.

[19] Z. Huang et al., "25 Gbps low-voltage waveguide Si-Ge avalanche photodiode," *Optica*, vol. 3, no. 8, pp. 793–798, Aug. 2016.

[20] M. Huang, P. Cai, L. Su, G. Hou, and P. Dong, "56 GHz waveguide Ge/Si avalanche photodiode," in *Proc. Opt. Fiber Commun. Conf.*, 2018, Paper. W4D.6.

[21] B. Wang et al., "A low-voltage Si-Ge avalanche photodiode for high-speed and energy efficient silicon photonic links," *J. Lightw. Technol.*, vol. 38, no. 12, pp. 3156–3163, Jun. 2020.

[22] L. Zhang et al., "A comparison of APD and SPAD based receivers for visible light communications," *J. Lightw. Technol.*, vol. 36, no. 12, pp. 2435–2442, Dec. 2018.

[23] N. Z. Hakim, B. E. Saleh, and M. C. Teich, "Signal-to-noise ratio for lightwave systems using avalanche potodiodes," *J. Lightw. Technol.*, vol. 9, no. 3, pp. 318–320, Mar. 1991.